Journal of Innovative Optical Health Sciences
Vol. 11, No. 2 (2018) 1750014 (9 pages)

DOI: 10.1142/S1793545817500146

Source reconstruction for bioluminescence tomography via $L_{1/2}$ regularization

Jingjing Yu*, Qiyue Li and Haiyu Wang
School of Physics and Information Technology
Shaanxi Normal University, Xi'an 710119, P. R. China
**yujj@snnu.edu.cn*

Received 23 December 2016
Accepted 6 March 2017
Published 26 April 2017

Bioluminescence tomography (BLT) is an important noninvasive optical molecular imaging modality in preclinical research. To improve the image quality, reconstruction algorithms have to deal with the inherent ill-posedness of BLT inverse problem. The sparse characteristic of bioluminescent sources in spatial distribution has been widely explored in BLT and many L_1-regularized methods have been investigated due to the sparsity-inducing properties of L_1 norm. In this paper, we present a reconstruction method based on $L_{1/2}$ regularization to enhance sparsity of BLT solution and solve the nonconvex $L_{1/2}$ norm problem by converting it to a series of weighted L1 homotopy minimization problems with iteratively updated weights. To assess the performance of the proposed reconstruction algorithm, simulations on a heterogeneous mouse model are designed to compare it with three representative sparse reconstruction algorithms, including the weighted interior-point, L1 homotopy, and the Stagewise Orthogonal Matching Pursuit algorithm. Simulation results show that the proposed method yield stable reconstruction results under different noise levels. Quantitative comparison results demonstrate that the proposed algorithm outperforms the competitor algorithms in location accuracy, multiple-source resolving and image quality.

Keywords: Bioluminescence tomography; $L_{1/2}$ regularization; inverse problem; reconstruction algorithm.

1. Introduction

Bioluminescence tomography (BLT) is a powerful preclinical imaging modality that localizes and quantifies internal bioluminescent sources with images of the light emitted through the animal surface. It provides a method of quantitative measuring and visualizing a range of molecular and cellular-level biological processes that occur *in vivo*

*Corresponding author.

in small animals with the help of bioluminescent reporters.[1–4] It has found a wide range of biomedical applications in drugs development and therapies evaluation for cancer researches.[5–8]

To reconstruct three-dimensional distributions of sources from the collected boundary measurements, both a forward model for simulating light transport and an elaborate inverse algorithm are required. Given a model describing light transport in tissue and the optical properties of the object to be imaged, the key problem of inverse algorithm is to deal with the severe ill-posedness of BLT and hence to produce efficient and stable reconstruction.

Regularization is an essential technique to stable the solution by combining a priori information into inverse problem solving. The sparse characteristic of bioluminescent sources in spatial distribution has been widely explored in BLT and many sparse regularization methods have been investigated.[3,4,9–11] Among them, L_1 regularization is the most popular one due to its efficiency. However, the study in the context of sparse signal recovery or compressed sensing has shown that L_p norm $(0 < p < 1)$ regularizations yield better solutions for sparse problems compared with L_1 norm.[11,12] Theoretical analysis and experimental results has proved that fewer measurements are enough for sparse signal recovery with L_p regularization. Besides, the $L_{1/2}$ regularization has been recognized as a representative of L_p $(0 < p < 1)$.[13]

Although the nonconvexity of L_p norm incur computational complexity with $p < 1$, L_p regularization has attracted considerable attention in various applications. In optical imaging, L_p regularization has been used in diffuse optical tomography (DOT)[14] for the improvement of image quality. Recently, nonconvex L_p regularizer find its place in fluorescence molecular tomography (FMT) for sparsity enhancement.[15–21] Chen *et al.* introduced L_p regularizer into BLT and proposed the weighted interior-point algorithm (WIPA) for solving the nonconvex optimization problem.[22]

In this paper, we present a $L_{1/2}$ norm-based reconstruction algorithm for BLT. Like the method proposed in Ref. 22, we solve the nonconvex objective function by converting it to a series of weighted L_1 minimization problems. Instead of interior-point method, a homotopy-based method is used in this paper to obtain fast and accurate solution of the reweighted L_1 problem and perform an internal "adaptive reweighting" after every homotopy step.

The paper is organized as follows. In Sec. 2, we briefly introduce the modeling of BLT and describe the proposed reconstruction method based on $L_{1/2}$ norm regularization in detail. Simulation experiments based on a heterogeneous mouse model are presented in Sec. 3. To assess the performance of the proposed algorithm, we compared our $L_{1/2}$ norm method with three representative sparse reconstruction algorithm, including the WIPA[22] for $L_{1/2}$ regularization, the homotopy method for L_1 minimization (L1 homotopy),[23] and the Stagewise Orthogonal Matching Pursuit (StOMP).[24]

2. Method

2.1. *Forward problem of BLT*

In this study, the diffusion approximation to radiative transport equation is used to depict the forward model. The diffusion equation (DE) with the Robin boundary condition is described as follows[3]:

$$-\nabla \cdot (D(r)\nabla B(r)) + \mu_a(r)B(r) = S(r)(r \in \Omega), \tag{1}$$

$$B(r) + 2A(r)D(r)(v(r) \cdot \nabla B(r)) = 0(r \in \partial\Omega), \tag{2}$$

where $r \in R^3$ represents the position, $S(r)$ describes the space and angle distribution of the internal source. $B(r)$ represents the power density at r, v is the outer normal vector on $\partial\Omega$, and $A(r)$ denotes the mismatch factor of boundary. In Eq. (1), $D(r) = 1/(3(\mu_a(r) + (1-g)\mu_s(r)))$ is the diffusion coefficient with g the anisotropy parameter, $\mu_a(r)$ being the absorption coefficient and $\mu_s(r)$ the scattering coefficient.

We can derive the following linear model by solving DE with the finite element method (FEM):

$$AX = B, \tag{3}$$

where A is a weight matrix that founds the relationship between the measurements and the unknowns. Vector X denotes the distribution of bioluminescent source and vector B represents the measurable boundary data.

2.2. *$L_{1/2}$ norm reconstruction method*

Equation (3) is an under-determined and ill-conditioned system, and thus various regularization techniques have been used to deal with the high ill-posedness of the inverse problem. For instance,

currently popular L_1 regularization methods formulate the BLT inverse problem as an optimization problem with L_1-norm penalty term:

$$\min_X \frac{1}{2}\|AX-B\|_2^2+\lambda\|X\|_1, \tag{4}$$

where λ denotes the regularization parameter and $\|X\|_1=\sum_{i=1}^{N}|x_i|$ is the L_1 norm.

To obtain better solutions, we use a $L_{1/2}$ regularization model for sparse BLT reconstruction. By replacing the L_1 norm term in Eq. (4) with $L_{1/2}$ quasi-norm penalty, we obtain the following $L_{1/2}$-regularized optimization model:

$$\min_X \frac{1}{2}\|AX-B\|_2^2+\lambda\|X\|_{\frac{1}{2}}^{\frac{1}{2}}, \tag{5}$$

where $\|X\|_{\frac{1}{2}}^{\frac{1}{2}}=\sum_{i=1}^{n}|x_i|^{\frac{1}{2}}$. The simplified form of Eq. (5) is

$$\min_X \frac{1}{2}\|AX-B\|_2^2+\lambda\sum_{i=1}^{n}|x_i|^{\frac{1}{2}}. \tag{6}$$

Unlike L_1 norm model, the objective with $L_{1/2}$ penalty is nonconvex and incurs computational complexity to the least squares problem in (6). Considerable effort has therefore been devoted to such nonconvex problems.[25] In this study, we employ an iterative reweighting method.[26,27]

Since $\sum_{i=1}^{n}|x_i|^{1/2}=\sum_{i=1}^{n}(1/\sqrt{|x_i|})|x_i|$, we can transform Eq. (6) to

$$\min_X \frac{1}{2}\|AX-B\|_2^2+\lambda\sum_{i=1}^{n}(1/\sqrt{|x_i|})|x_i|. \tag{7}$$

Thus, we obtain a weighted L_1-norm problem which we can solve it iteratively.[13] Let $w_i=\frac{\lambda}{\sqrt{|x_i^t|}}$, we get:

$$X^{t+1}=\arg\min_X \frac{1}{2}\|AX-B\|_2^2+\sum_{i=1}^{n}w_i|x_i|. \tag{8}$$

In this way, the intractable $L_{1/2}$ norm problem is converted into a series of weighted L_1 minimization. For sparse reconstruction problem, there exist many zero elements in X. To guarantee numerical stability, we take $w_i=\frac{\lambda}{\sqrt{|x_i^t|}+\tau}$ in our implementation, where τ is a small number.

In a common iterative reweighting approach, we need re-compute weights at every iteration using the solution X at the previous iteration. To obtain fast and accurate solution of the reweighted L_1 problem in (8), we employ the homotopy-based algorithm to perform an internal "adaptive reweighting" after every homotopy step. Therefore, the following homotopy program was used:

$$\min_X \frac{1}{2}\|AX-B\|_2^2+\sum_{i=1}^{n}((1-\sigma)w_t+\sigma w_{t+1})|x_i|, \tag{9}$$

where σ is a homotopy parameter and when it changes from 0 to 1, the new weight phase in and the old one phase out. At any value of σ, the X^* must satisfy the following optimality conditions[28]:

$$a_i^T(AX^*-B)=-((1-\sigma)w_t+\sigma w_{t+1})z_i \quad \text{for all} \quad i\in\Gamma \tag{10a}$$

$$|a_i^T(AX^*-B)|<-(1-\sigma)w_t+\sigma w_{t+1} \quad \text{for all} \quad i\in\Gamma^c, \tag{10b}$$

where Γ denotes the support of X^*, a_i is ith column of A and z denotes the sign sequence of X^*. When increase σ up to $\sigma+\delta$, the ∂X will direct the moving of solution, and the optimality condition will change to:

$$A_\Gamma^T(AX^*-B)+\delta A_\Gamma^T A\partial X=-((1-\sigma)W_t+\sigma W_{t+1})z+\delta(W_t-W_{t+1})z \tag{11a}$$

$$\left\|\underbrace{a_i^T(AX^*-\Phi)}_{pi}+\delta\underbrace{a_i^T A\partial x}_{di}\right\|_\infty \le \underbrace{(1-\sigma)w_t+\sigma w_{t+1}}_{qi}+\delta\underbrace{(w_t+w_{t+1})}_{si}, \tag{11b}$$

where W_t and W_{t+1} are $|\Gamma|\times|\Gamma|$ diagonal matrices with diagonal entries being the values of w_t and w_{t+1} on Γ, respectively. And the update direction specified by the conditions (11a) as:

$$\partial X=\begin{cases}(A_\Gamma^T A_\Gamma)^{-1}(W_t-W_{t+1})z & \text{on} \quad \Gamma\\ 0 & \text{on} \quad \Gamma^c\end{cases}. \tag{12}$$

When we increase δ, the solution moves based on the direction ∂X until either a new element enters the support of solution or an existing element turns to 0. The step-size that takes the solution to such a critical value of σ can be computed as

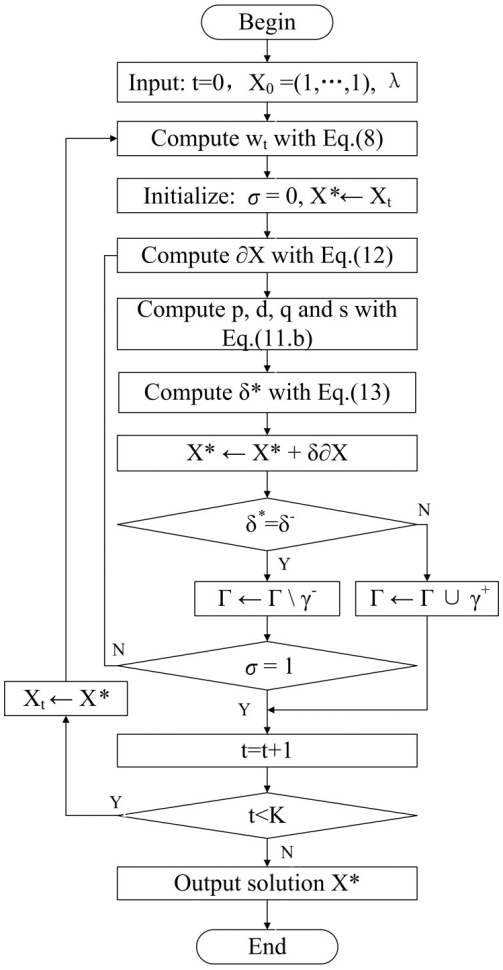

Fig. 1. Flow chart of the IRW-$L_{1/2}$ algorithm.

$\delta^* = \min(\delta^+, \delta^-)$, where:

$$\delta^+ = \min_{i\in\Gamma^c}\left(\frac{q_i - p_i}{-s_i + d_i}, \frac{-q_i - p_i}{s_i + d_i}\right)_+, \qquad (13)$$
$$\delta^- = \min_{i\in\Gamma}\left(\frac{-x_i^*}{\partial x_i}\right)_+$$

δ^+ is the smallest step-size that makes a constraint in (11b) active, indicating entry of a new element in the support, whereas δ^- is the smallest step-size that shrinks an existing element at γ^- to 0. The new critical value of σ turns to $\sigma + \delta^*$, the solution X^* turns to $X^* + \delta^*\partial X$, where the support and sign sequence are updated accordingly. At each homotopy step, we jump from one value of σ to the next while updating the support of the solution, until $\sigma = 1$.

In our experiment, we set the initial solution as $X^0 = (1, \ldots, 1)$, which means that we use the solution of the L1 homotopy algorithm as the first iteration solution. The iterative reconstruction algorithm will stop when the iteration number t reaches the maximum iteration limit K ($K = 10$ for the following simulations). Figure 1 describes the specific steps of the proposed reconstruction algorithm (IRW-$L_{1/2}$, for short).

Table 1. Optical parameters for the mouse organs.

Tissues	Muscle	Lungs	Heart	Liver	Kidneys	Stomach
μ_a [mm^{-1}]	0.23	0.35	0.11	0.45	0.12	0.21
μ_s' [mm^{-1}]	1.00	2.30	1.10	2.00	1.20	1.70

3. Simulation Studies on the Mouse Atlas

In this section, a series of simulations on a digimouse model were conducted to assess the performance of the proposed reconstruction algorithm IRW-$L_{1/2}$. For comparison, we chose three representative algorithms to investigate, including the WIPA, L1 homotopy and StOMP. The mouse atlas is a digital mouse which provides anatomical information.[29] The optical properties of digimouse are listed in Table 1.[30] The body section with a length of 34 mm was selected in the following simulations.

Several groups of simulations were designed to assess the location accuracy and source resolving ability of the four testing algorithms in single-source and double-source reconstruction scenarios. We also investigated the influence of measurement noise and optical properties of tissues on the algorithms with single-source simulations.

The reconstruction results were evaluated by not only visual inspection but also quantitative metrics

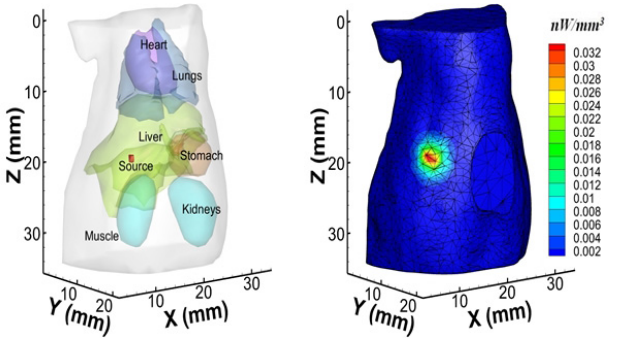

(a) (b)

Fig. 2. (a) The torso of the mouse atlas model with a cylindrical source in the liver, (b) forward mesh and the simulated photon distribution on the surface.

Table 2. Reconstructed location error under different noise levels (mm) in single-source case.

Method \ Noise level	0%	5%	10%	15%
IRW-$L_{1/2}$	0.48064	0.48064	0.48067	0.48070
WIPA	0.51805	0.51804	0.51803	0.51811
L1 homotopy	0.52492	0.52491	0.52498	0.52057
StOMP	0.50179	0.50180	0.50179	0.50178

Table 3. CNR under different noise levels in single-source case.

Method \ Noise level	0%	5%	10%	15%
IRW-$L_{1/2}$	12.5196	12.5196	12.5204	12.5212
WIPA	8.2055	8.2057	8.2014	8.1959
L1 homotopy	10.0940	10.0945	10.0945	10.0917
StOMP	11.8834	11.8835	11.8836	11.8831

including location error (LE) and contrast-to-noise ratio (CNR) of the reconstructed image. LE is the distance between the reconstructed source center and the actual one. CNR is defined as follows[31]:

$$\mathrm{CNR} = \frac{\mu_{\mathrm{ROI}} - \mu_{\mathrm{BCK}}}{[\omega_{\mathrm{ROI}}\sigma^2_{\mathrm{ROI}} + \omega_{\mathrm{BCK}}\sigma^2_{\mathrm{BCK}}]^{1/2}}, \tag{14}$$

where μ_{ROI} is the mean values of the ROI (the region of interest) and μ_{BCK} is the mean values of the variable background. σ_{ROI} and σ_{BCK} are the standard deviations of the ROI and background, respectively. ω_{ROI} and ω_{BCK} are weighting factors.

The algorithms were coded in Matlab™ and operated on a PC with 3.3 GHz Intel® Core™ i5-4590 and 8GB RAM. The threshold for StOMP and the regularization parameters for WIPA, IRW-$L_{1/2}$ and L1 homotopy were selected manually in the following simulations.

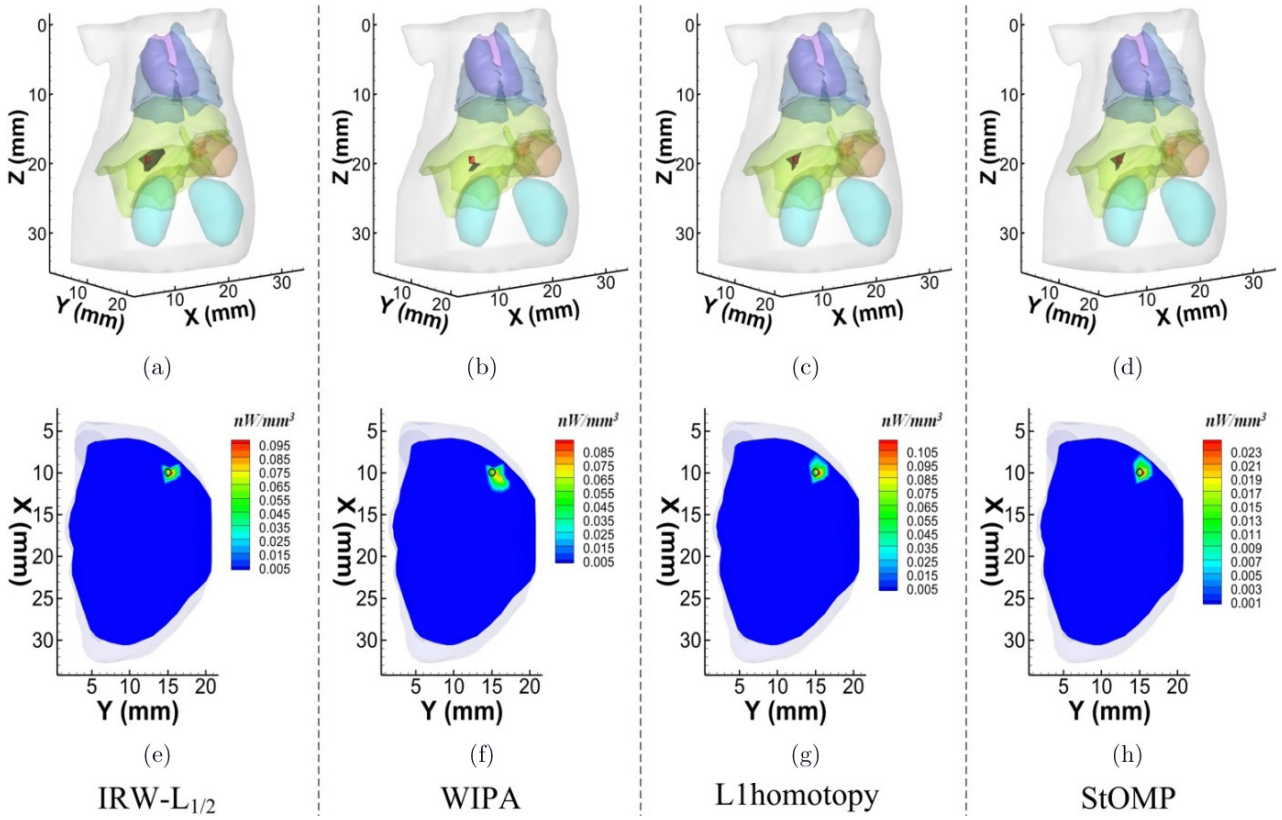

Fig. 3. Reconstruction results by the four algorithms in single-source simulation. The top row shows the 3D views of results by IRW-$L_{1/2}$, WIPA, L1 homotopy and StOMP, respectively. The bottom row shows the corresponding transverse views at $z = 18$ mm, where the actual source center located.

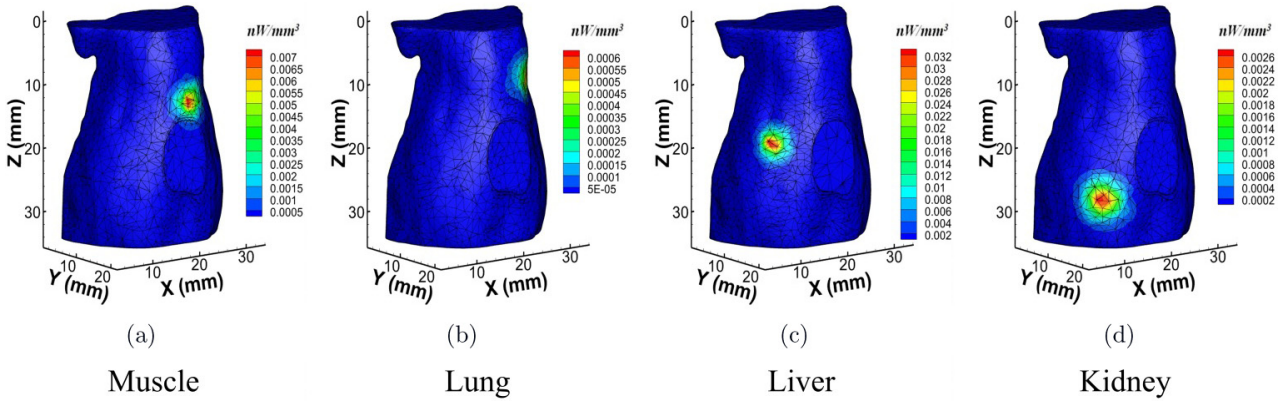

Fig. 4. Simulated photon distribution on the surface for single-source located in different tissues.

3.1. *Reconstruction of single-source*

In the first group of simulations, a cylindrical source was put in the liver, as shown in Fig. 2(a). The source with a radius of 0.5 mm and height of 1 mm centered at (10 mm, 15 mm, 18 mm). And the magnitude of the actual source was set to be $1\,\mathrm{nW/mm^3}$.

To obtain simulated measurements, the mouse model (with source) was discretized into a FEM mesh including 99340 tetrahedral elements and 17956 nodes. Figure 2(b) exhibits the surface distribution. A coarser mesh consisted of 16755 elements and 3201 nodes were used for reconstruction, and we used all of the surface measurements of the torso section to reconstruct the target with the four algorithms. Besides, different levels (5–15%) of Gaussian noise were added to the simulated measurement to test the stability of reconstruction algorithms.

Tables 2 and 3 summarize the average LE and CNR of 10 times running of each algorithm under different noise levels (except the noiseless case), respectively. Figure 3 shows the transverse views at $z = 18$ mm and 3D views of the reconstruction results in noiseless case. From Tables 2 and 3, we observed very small fluctuation for all the testing algorithms, which means all reconstruction algorithms performed quite stable under noise conditions. However, quantitative comparison results shown in tables demonstrate that the proposed IRW-$L_{1/2}$ algorithm slightly outperformed the competitors in location accuracy and image quality in single-source case.

3.2. *Reconstruction single-source located in different tissues*

Considering that the optical properties and depth of the source vary from tissue to tissue, we designed a

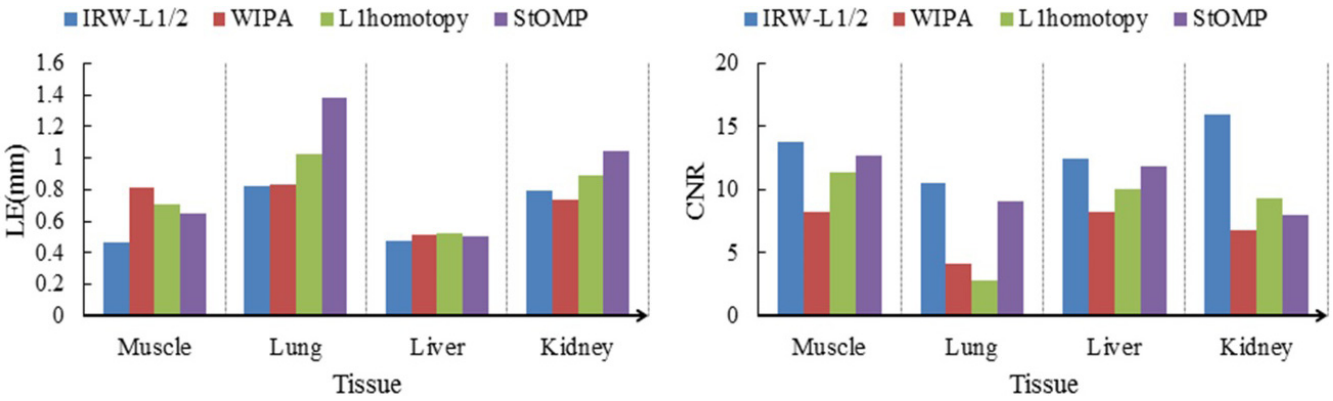

Fig. 5. Comparison results in reconstruction of single-target located in different tissues (a) Location error. (b) CNR.

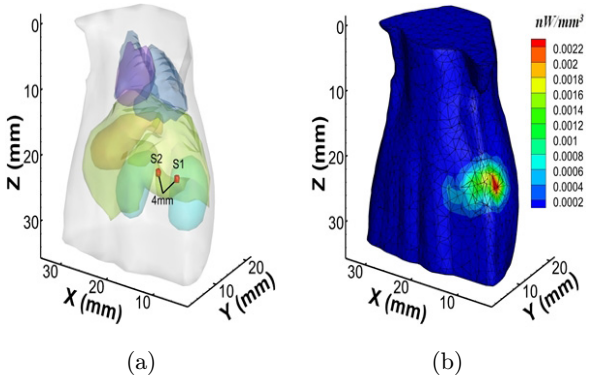

Fig. 6. (a) Source setting and (b) the simulated photon distribution on the surface in double-source case.

group of simulations to investigate the performance of the algorithms in reconstructing single-target located in different tissues. We tested four cases with a same source placed in muscle, lung, liver and kidney, respectively. Figure 4 shows the simulated photon distribution on the surface for single-source located in different tissues. Figure 5 plots the comparison results of the algorithms in location error and CNR. We observed that IRW-$L_{1/2}$ outperformed WIPA, L1 homotopy and StOMP in the most of the different cases.

3.3. *Reconstruction of double-source*

In this case, two identical cylindrical sources were placed at S1=(9,7,20 mm) and S2=(13,7,20 mm) in liver, with a 4 mm separation distance between centers. In forward calculation, the mouse model with double-source was discretized into a mesh including 103813 elements and 18634 nodes. Figure 6 exhibits the source setting and the simulated surface distribution in this case. The mesh used for reconstruction consisted of 15957 elements and 3042 nodes. Since the results in Sec. 3.1 show that measurement noise had less impact on the four testing algorithms, the following reconstructions were conducted under noise free condition.

Figure 7 shows that reconstructed result by the four different algorithms. From Fig. 7, we observed that the two targets reconstructed by IRW-$L_{1/2}$ concentrate in two localized regions close to actual

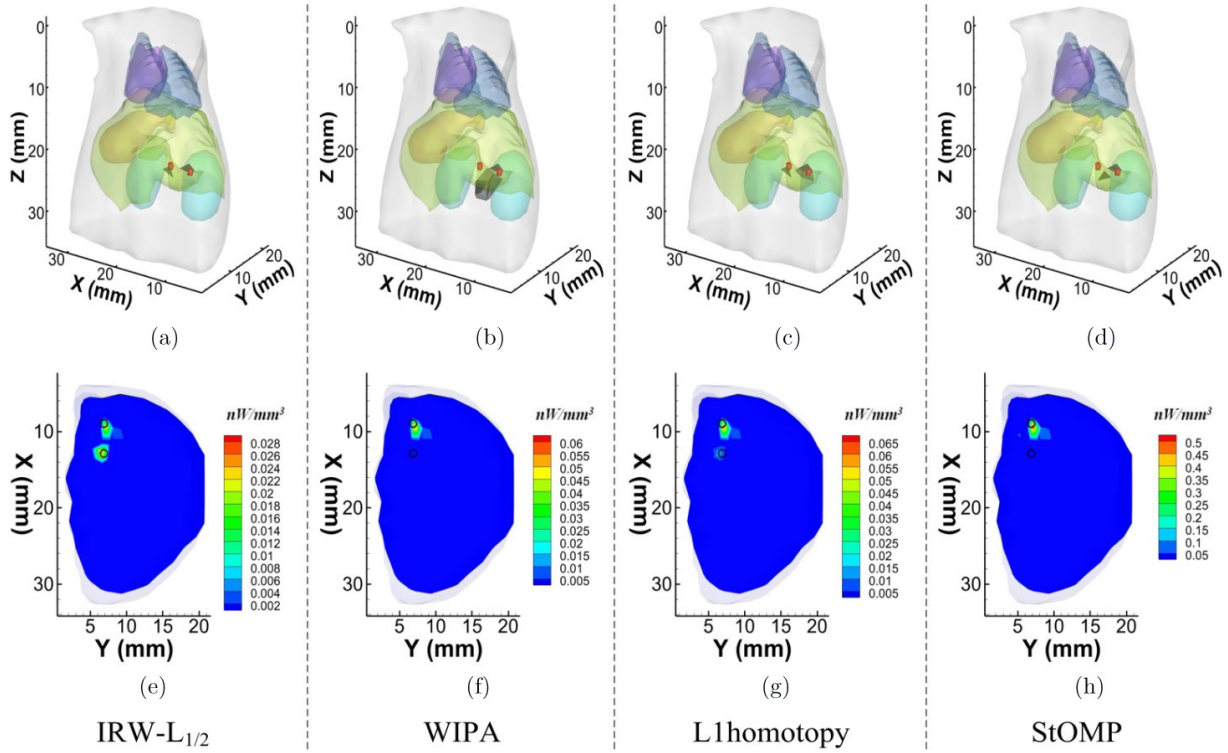

Fig. 7. Reconstruction results by the four algorithms in double-source simulation. The top row shows the 3D views of results by IRW-$L_{1/2}$, WIPA, L1 homotopy and StOMP, respectively. The bottom row shows the corresponding transverse views at $z = 20$ mm, where the actual source centers located.

Table 4. Quantitative reconstruction results in double-sources case.

Method	Source	Actual center (mm)	Recon. center (mm)	LE (mm)	CNR
IRW-$L_{1/2}$	S1	(9,7,20)	(9.36,7.15,19.99)	0.454	5.98
	S2	(13,7,20)	(12.88,6.40,19.95)	0.617	
WIPA	S1	(9,7,20)	(9.39, 7.20, 19.90)	0.451	4.03
	S2	(13,7,20)	(12.068.0622.51)	2.883	
L1 homotopy	S1	(9,7,20)	(9.39,7.19,19.96)	0.433	5.48
	S2	(13,7,20)	(12.95,6.22,20.39)	0.871	
StOMP	S1	(9,7,20)	(9.42,7.21,19.84)	0.502	5.73
	S2	(13,7,20)	(11.53,6.04,20.97)	1.998	

source centers. Nevertheless, there exist larger deviations in the results by WIPA, L1 homotopy and StOMP. Table 4 summarized the quantitative results in terms of reconstructed source centers, location error for each source and CNR. The results shown in Fig. 7 and Table 4 demonstrate that IRW-$L_{1/2}$ significantly outperformed the other competitors in double-source case.

4. Discussion and Conclusion

This paper presents an efficient source reconstruction method for BLT based on $L_{1/2}$ regularization. Due to the nonconvexity of the objective, we convert the $L_{1/2}$-regularized problem into a series of L_1 minimization problems by iterative reweighting approach, and perform a homotopy-based algorithm to obtain fast and accurate reconstruction.

The simulation results for single-source reconstruction on a digital mouse model indicate that the proposed source reconstruction method IRW-$L_{1/2}$ outperforms the three representative sparse algorithms in location accuracy and CNR. The simulation results under different noise levels and different tissues show the stability of the proposed method. The double-source case results also demonstrate the superiority of the IRW-$L_{1/2}$ in resolving multiple sources.

Although the simulation results based on animal atlas are competitive, further investigations with phantom and in vivo experiments are necessary for an overall assessment of the proposed method, which will be one of our future works. On the basis of the simulations, we speculate that the proposed IRW-$L_{1/2}$ is a promising reconstruction method for BLT applications.

Acknowledgments

This work was supported by the National Natural Science Foundation of China (No. 61401264, 11574192), the Natural Science Research Plan Program in Shaanxi Province of China (No. 2015JM6322), and the Fundamental Research Funds for the Central Universities (No. GK201603025).

References

1. C. Darne, Y. Lu, E. M. Sevick-Muraca, "Small animal fluorescence and bioluminescence tomography: A review of approaches, algorithms and technology update," *Phys. Med. Biol.* **59**, R1 (2014).
2. C. Qin, J. Feng, S. Zhu, X. Ma, J. Zhong, P. Wu, Z. Jin, J. Tian, "Recent advances in bioluminescence tomography: Methodology and system as well as application," *Laser Photon. Rev.* **8**, 94–114 (2014).
3. W. Cong, G. Wang, D. Kumar, Y. Liu, M. Jiang, L. V. Wang, E. A. Hoffman, G. McLennan, P. B. McCray, J. Zabner, A. Cong, "Practical reconstruction method for bioluminescence tomography," *Opt. Express* **13**, 6756–6771 (2005).
4. X. He, J. Liang, X. Wang, J. Yu, X. Qu, X. Wang, Y. Hou, D. Chen, F. Liu, J. Tian, "Sparse reconstruction for quantitative bioluminescence tomography based on the incomplete variables truncated conjugate gradient method," *Opt. Express* **18**, 24825–24841 (2010).
5. H. Gao, H. Zhao, "Multilevel bioluminescence tomography based on radiative transfer equation Part 1: l1 regularization," *Opt. Express* **18**, 1854–1871 (2010).
6. J. Yu, B. Zhang, I. Iordachita, J. Reyes, Z. Lu, M. Brock, M. Patterson, J. Wong, K. Wong, "Systematic study of target localization for bioluminescence tomography guided radiation therapy," *Med. Phys.* **43**, 2619–2629 (2016).

7. X. Ma, J. Tian, C. Qin, X. Yang, B. Zhang, Z. Xue, X. Zhang, D. Han, D. Dong, X. Liu. "Early detection of liver cancer based on bioluminescence tomography," *Appl. Opt.* **50**, 1389–1395 (2011).
8. S. Mollard, R. Fanciullino, S. Giacometti, C. Serdjebi, S. Benzekry, J. Ciccolini, "In vivo bioluminescence tomography for monitoring breast tumor growth and metastatic spreading: Comparative study and mathematical modeling," *Sci. Rep.* **6**, 36173 (2016).
9. W. Guo, K. Jia, D. Han, Q. Zhang, X. Liu, J. Feng, C. Qin, X. Ma, J. Tian, "Efficient sparse reconstruction algorithm for bioluminescence tomography based on duality and variable splitting," *Appl. Opt.* **51**, 5676–5685 (2012).
10. J. Yu, F. Liu, J. Wu, L. Jiao, X. He, "Fast source reconstruction for bioluminescence tomography based on sparse regularization," *IEEE Trans. Biomed. Eng.* **57**, 2583–2586 (2010).
11. M. Yukawa, S. Amari, "Lp-regularized least squares $(0 < p < 1)$ and critical path," *IEEE Trans. Inf. Theory.* **62**, 488–502 (2016).
12. M. Lai, J. Wang, "An unconstrained ℓq minimization with $0 < q < 1$ for sparse solution of under-determined linear systems," *SIAM* **21**, 82–101 (2011).
13. Z. Xu, X. Chang, F. Xu, H. Zhang, "L1/2 regularization: A thresholding representation theory and a fast solver," *IEEE Trans. Neural Netw.* **23**, 1013–1027 (2012).
14. S. Okawa, Y. Hoshi, Y. Yamada, "Improvement of image quality of time-domain diffuse optical tomography with lp sparsity regularization," *Biomed. Opt. Express* **2**, 3334–3348 (2011).
15. W. Xie, Y. Deng, K. Wang, X. Yang, Q. Luo, "Reweighted L1 regularization for restraining artifacts in FMT reconstruction images with limited measurements," *Opt. Lett.* **39**, 4148–4151 (2014).
16. D. Zhu, C. Li, "Nonconvex regularizations in fluorescence molecular tomography for sparsity enhancement," *Phys. Med. Biol.* **59**, 2901–2912 (2014).
17. H. Guo, J. Yu, X. He, Y. Hou, F. Dong, S. Zhang, "Improved sparse reconstruction for fluorescence molecular tomography with L1/2 regularization," *Biomed. Opt. Express* **6**, 1648–1664 (2015).
18. J. Shi, F. Liu, H. Pu, S. Zuo, J. Luo, J. Bai, "An adaptive support driven reweighted L1-regularization algorithm for fluorescence molecular tomography," *Biomed. Opt. Express* **5**, 4039–4052 (2014).
19. L. Lian, Y. Deng, W. Xie, G. Xu, X. Yang, Z. Zhang, Q. Luo, "High-dynamic-range fluorescence molecular tomography for imaging of fluorescent targets with large concentration differences," *Opt. Express* **24**, 19920–19933 (2016).
20. J. Shi, F. Liu, J. Zhang, J. Luo, J. Bai, "Fluorescence molecular tomography reconstruction via discrete cosine transform-based regularization," *J. Biomed. Opt.* **20**, 055004 (2015).
21. H. Zhang, G. Geng, X. Wang, X. Qu, Y. Hou, X. He, "Fast and robust reconstruction for fluorescence molecular tomography via L1-2 regularization," *Biomed. Res. Int.* **2016**, 5065217 (2016).
22. X. Chen, D. Yang, Q. Zhang, J. Liang, "L1/2 regularization based numerical method for effective reconstruction of bioluminescence tomography," *Appl. Phys.* **115**, 184702 (2014).
23. M. R. Osborne, B. A. Turlach, "A homotopy algorithm for the quantile regression lasso and related piecewise linear problems," *J. Comput. Graph. Statist.* **20**, 972–987 (2011).
24. D. L. Donoho, Y. Tsaig, I. Drori, J. L. Starck, "Sparsesolution of underdetermined linear equations by stagewise orthogonal matching pursuit," *IEEE Trans. Inf. Theory.* **58**, 1094–1121 (2012).
25. R. Chartrand, V. Staneva, "Restricted isometry properties and nonconvex compressive sensing," *Inverse Probl.* **24**, 1–14 (2008).
26. E. J. Candes, M. B. Wakin, S. P. Boyd, "Enhancing sparsity by reweighted L1 minimization," *J. Fourier Anal. Appl.* **14**, 877–905 (2008).
27. M. Asif, J. Romberg, "Fast and accurate algorithms for re-weighted L1-norm minimization," *IEEE Trans. Signal Process.* **61**, 5905–5916 (2013).
28. J. Fuchs, "On sparse representations in arbitrary redundant bases," *IEEE Trans. Inf. Theory* **50**, 1341–1344 (2004).
29. B. Dogdas, D. Stout, A. F. Chatziioannou, R. M. Leahy, "Digimouse: A 3D whole body mouse atlas from CT and cryosection data," *Phys. Med. Biol.* **52**, 577–587 (2007).
30. G. Wang, W. Cong, K. Durairaj, X. Qian, H. Shen, P. Sinn, E. Hoffman, G. McLennan, M. Henry, "In vivo mouse studies with bioluminescence tomography," *Opt. Express* **14**, 7801–7809 (2006).
31. X. Song, B. Pogue, S. Jiang, M. Doyley, H. Dehghani, T. Tosteson, K. Paulsen, "Automated region detection based on the contrast-to-noise ratio in near-infrared tomography," *Appl. Opt.* **43**, 1053–1062 (2004).